

## Self-Standing N-Doped Carbonized Cellulose Fiber as a Dual-Functional Host for Lithium Metal Anodes

Zhipeng Wen, Huiyang Li, Jiaxiang Liu, Yang Yang,\* and Jinbao Zhao\*

Cite This: *ACS Sustainable Chem. Eng.* 2021, 9, 2326–2337

Read Online

ACCESS |



Metrics &amp; More



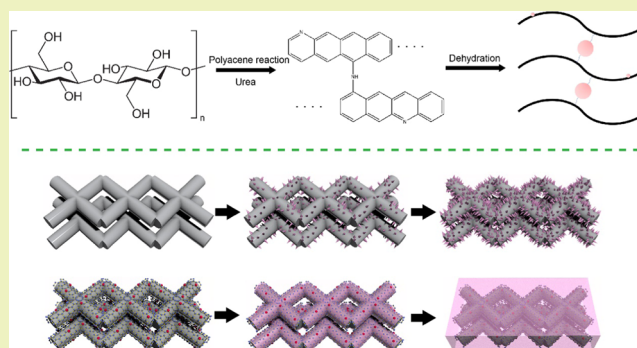
Article Recommendations



Supporting Information

**ABSTRACT:** Lithium (Li) metal is regarded as the holy grail among various anode candidates due to its extremely high specific energy and low electrochemical potential. Nevertheless, uncontrolled dendrite growth and an unstable electrode/electrolyte interface become the bottleneck for the development of rechargeable Li metal batteries. Although many research studies have focused on designing porous electrode architectures to reduce the local current density and delay the Li dendrite growth, constructing a stable reaction interface is still highly desired. Herein, we ingeniously designed a facile immersion and subsequent annealing method to fabricate a nitrogen-doped carbonized cellulose fiber (N-CF). The nitrogen element can not only bridge the polyacene reaction of cellulose in the process of lower calcination temperatures to improve the mechanical strength but also improve the lithophilic property of a current collector by nitrogen doping at higher calcination temperatures. Therefore, the as-synthesized N-CF can maintain good structural integrity during the cycle and promote the stability of the electrode/electrolyte interface. As a result, when matched with a commercial  $\text{LiNi}_{0.5}\text{Co}_{0.2}\text{Mn}_{0.3}\text{O}_2$  cathode, the capacity retention of a N-CF// $\text{LiNi}_{0.5}\text{Co}_{0.2}\text{Mn}_{0.3}\text{O}_2$  full cell can reach as high as 83.1% after 250 cycles. Our work reveals a facile approach to regulate the Li deposition behavior and stabilize the electrode/electrolyte interface simultaneously.

**KEYWORDS:** dual-functional, polyacene reaction bridge, nitrogen doping, Li metal anode, commercial  $\text{LiNi}_{0.5}\text{Co}_{0.2}\text{Mn}_{0.3}\text{O}_2$  cathode



## INTRODUCTION

The development of the electrochemical energy storage technology has always been closely related to people's production and life. Since the first commercial production of LIBs with a graphite anode by SONY Corporation in 1991, LIBs have quickly penetrated all aspects of our lives.<sup>1,2</sup> However, the current LIBs are gradually unable to meet requirements of energy storage systems in terms of energy density with the rapid progress of electric vehicles.<sup>3</sup> Compared with the graphite anodes currently applied in commercial LIBs, lithium (Li) metal has the lowest reduction potential ( $-3.04$  V vs SHE) and extremely high energy density ( $3860$  mAh  $\text{g}^{-1}$ ); thus, it can provide higher energy density. At present, only by increasing the energy density of lithium-based batteries to  $500$  Wh  $\text{kg}^{-1}$ , electric vehicles can form a certain competitiveness for fuel vehicles in the car market. To achieve this goal, most researchers believe that the use of Li metal anodes paired with metal oxides, oxygen ( $\text{Li}-\text{O}_2$ ),<sup>4–6</sup> and sulfur ( $\text{Li}-\text{S}$ )<sup>7</sup> may be the ultimate solution. From this perspective, the research of Li metal has great significance in the energy storage system.

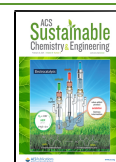
Although Li metal anode possesses various advantages, the limited cycle life and potential risks of Li dendrite formation severely restrict its practical application.<sup>8,9</sup> The issues of a Li

metal anode stem from the host-less deposition and stripping processes. During the deposition, the highly reactive Li metal easily reacts with the electrolyte to form a solid electrolyte interface (SEI) layer on the surface. Even worse, the formed SEI is very fragile and easily damaged by Li metal volume expansion, generating fresh Li metal exposed to the electrolyte and a new electrode/electrolyte interface.<sup>10</sup> The repeated generation and destruction of the SEI layer irreversibly consumes the amount of the Li metal and the electrolyte. In addition, the unevenness of the interface results in the formation of Li dendrites clearly. Li dendrites may pierce the separator during cycling and lead to the short-circuiting, even causing safety accidents. During the stripping process, Li metal tends to dissolve from the root. As a result, an amount of Li metal detaches and becomes dead Li, leading to the extremely low Coulombic efficiency. To sum up, the limited cycle life and

Received: November 23, 2020

Revised: December 21, 2020

Published: January 27, 2021



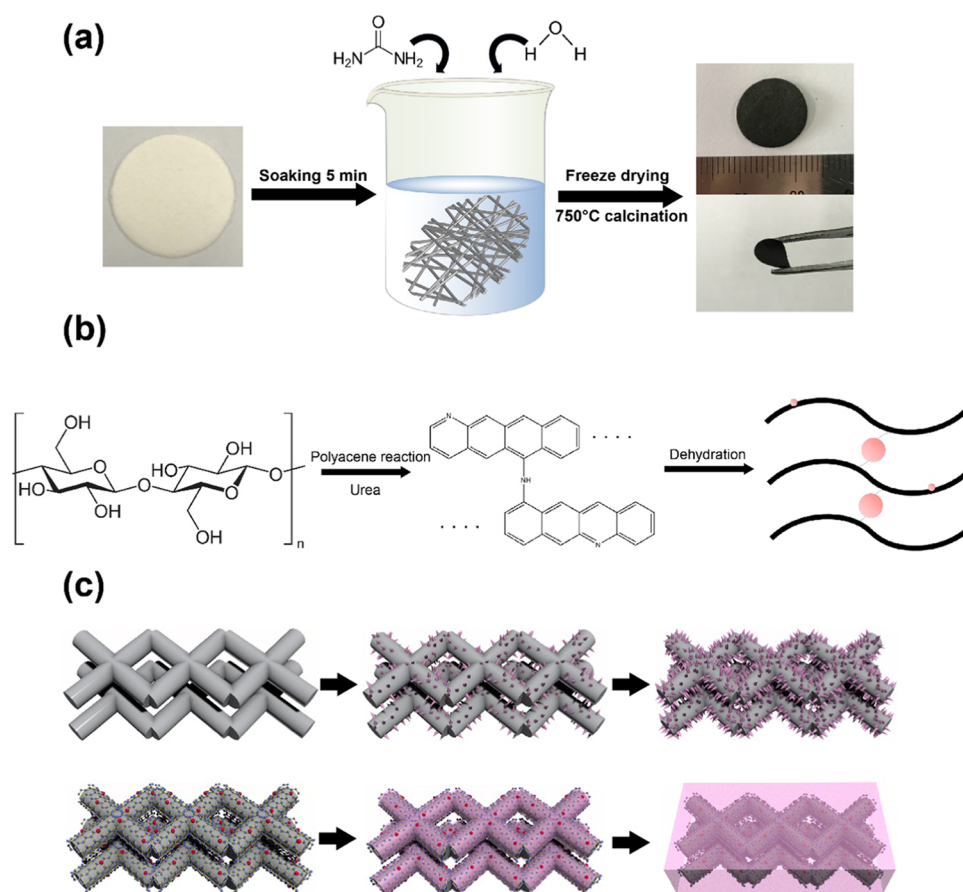


**Figure 1.** (a) Synthesis process diagram and the bending experiment optical image of N-CF. (b) The schematic diagram of the reaction process of cellulose after adding urea under a calcination temperature of 750 °C. (c) The schematic diagram of different Li metal deposition behaviors of CF and N-CF.

Li dendrites are the two main factors that restrict the evolution of Li-metal-based batteries.<sup>11</sup>

So far, many researchers have devoted themselves to improving the cycling performance of Li metal anodes from the perspective of improving the stability of the electrode/electrolyte interface and constraining the Li dendrites. In a traditional electrolyte environment, the native SEI on Li metal is very rigid, and it is easy to crack due to the volume expansion of Li metal. Therefore, the use of functional additives, such as CsPF<sub>6</sub>,<sup>12</sup> Li<sub>2</sub>S,<sup>13</sup> and VEC,<sup>14</sup> can modify the composition of SEI. The newly generated SEI can have certain flexibility to relieve the volume expansion, and the high Li-ion conductivity reduces polarization. Alternatively, the protective layer can be formed on a Li foil by physical methods or chemical methods in advance. The choice of the artificial protective layer is versatile, including Li<sub>3</sub>N,<sup>15</sup> LiI,<sup>16</sup> LiF,<sup>17</sup> etc. These modification strategies are based on constructing a stable interface between SEI and Li metal to achieve uniform Li metal deposition.<sup>18,19</sup>

The three-dimensional structure of a conductive matrix is often used to alleviate the formation of Li dendrites because it has a large specific surface area that can effectively reduce the local current density of Li deposition. Moreover, its voids can effectively relieve volume change before and after charging and discharging, such as VGCF,<sup>20</sup> nickel foam,<sup>21</sup> copper foam,<sup>22</sup> etc. In addition, improving the affinity of the current collector and Li metal can effectively make the electrodeposition more uniform and reduce the generation of Li dendrites. However,

only the three-dimensional conductive matrix cannot change the interface problems encountered during Li deposition, so the improvement of Coulombic efficiency is always limited.<sup>23–26</sup> Taking it into account, the strategy that combines the three-dimensional conductive matrix and improves the interface between SEI and the current collector is necessary to achieve long cycling and high deposition stripping efficiency simultaneously.<sup>27–29</sup>

In this work, we design a nitrogen-doped carbonized cellulose fiber (N-CF) conductive matrix through the bridge reaction of polyacene to achieve long cycling and high depositing/stripping efficiency of Li metal in a carbonate-ester electrolyte environment. The N-CF maintains the original 3D network structure and forms a conductive network. The surface fibrosis caused by nitrogen doping can effectively homogenize the distribution of Li ions on the surface, greatly reducing the concentration polarization. Moreover, the nitrogen-doped sites can effectively induce uniform Li deposition due to the lithophilic property. Benefiting from the bridging reaction of nitrogen (Figure 1b), N-CF exhibits excellent mechanical strength and flexibility (photographs in Figure 1a). Therefore, the N-CF combines the advantages of a three-dimensional conductive matrix and nitrogen doping-induced uniform Li metal deposition (Figure 1c) so that it can simultaneously suppress the Li dendrites and stabilize the electrode/electrolyte interface. In contrast, the carbonized cellulose fiber (CF) does not change the interface between SEI

and the current collector, so it experiences uncontrolled Li dendrite formation.

## EXPERIMENTAL SECTION

**Synthesis of CF and N-CF Current Collectors.** Initially, the cellulose fiber was purchased from Whatman company (6  $\mu\text{m}$  in pore diameter, 390  $\mu\text{m}$  in thickness), and cut into a circular disk (diameter, 12 mm) for preparation. During the preparation of the CF current collector process, the cellulose fiber was directly placed in a tube furnace and heated at 750  $^{\circ}\text{C}$  for 6 h at a heating rate of 3  $^{\circ}\text{C}/\text{min}$ . After natural cooling, the CF current collector was directly obtained. In the synthesis of a N-CF current collector, 50 g of urea was dissolved in 50 mL of deionized water and the solution was stirred about 5 min to completely dissolve. Then, the cellulose fiber disk was added into the high concentration urea solution, and it must be ensured that the cellulose fiber is completely submerged. After waiting for 5 min, the quality of urea remaining on the cellulose fiber can be stabilized at 0.07 g, indicating the complete absorption. Then, it can be taken out to remove moisture by freeze drying for 24 h. Then, the cellulose fiber filled with urea was heated at 750  $^{\circ}\text{C}$  for 6 h. After natural cooling, the N-CF current collector can be obtained.

**Material Characterization.** The morphology of an electrode structure and Li metal deposition are both studied using an electron scanning microscope (SEM); the acceleration voltage was controlled at 15 kV and the probe current was controlled at 10  $\mu\text{A}$  (Hitachi 4800). The characterization of the valence state of the CF current collector before and after nitrogen doping was carried out by an X-ray photoelectron spectroscopy analyzer (XPS, PHI QUANTUM 2000). The electrochemical impedance spectroscopy (EIS) was measured by the Autolab PGSTAT 101 with the frequency range of 10 mHz to 100 kHz and had also been fitted by an equivalent circuit. The nitrogen adsorption and desorption isotherms were attained on a micromeritics surface area and porosity analyzer (BET, ASAP-2020, Micromeritics). To accurately measure the electronic conductivity of the current collector, the electrical conductivity was measured on a four-point probe powder resistivity meter (SZT-D, Suzhou Jingge Electronics Co., Ltd.). To obtain the structural information of CF and N-CF current collectors, a confocal microscopic Raman spectrometer XploRA (Horiba, Japan) was employed. The elemental content analysis test was carried out using an elemental analyzer (Vario EL III, Germany). The Fourier transform infrared (FTIR) spectra were collected using a Nicolet IS5 spectrometer (Thermo Fisher).

**Electrochemical Measurements.** Above the entire electrochemical performance measurements, the CR2032 button cell was selected to test. The cell assembly process was carried out in a glovebox (water content below 0.5 ppm, oxygen content below 0.5 ppm). For the cell assembly, the ester electrolyte that owns a higher voltage window was selected, which was configured by ethylene carbonate (EC) and dimethyl carbonate (DMC) in a volume ratio of 1:1. Lithium hexafluorophosphate ( $\text{LiPF}_6$ ) (1 M) was used as the lithium salt together with additional 2% of vinylene carbonate (VC). Toward all-cell assembly processes mentioned in this paper, the electrolyte consumption was 100  $\mu\text{L}$ .

When measuring the Coulombic efficiency, the CF or N-CF was used as a working electrode, and the Li foil was used as a counter electrode. After assembling the Li-CF half-cell, the initial SEI was constructed by circulating four cycles with voltage ranging from 0 to 1 V.

To test the performance of a Li symmetric cell, CF or N-CF predeposited with 10  $\text{mAh cm}^{-2}$  Li metal was used for preparation. After the electrodeposition had been completed, the CF-Li current collector was taken out and the Li metal symmetric cell was assembled. The Li metal deposition amount of the symmetric cell performance test was controlled at 1  $\text{mAh cm}^{-2}$  and the current density was selected to be 0.5  $\text{mA cm}^{-2}$ .

During the full-cell performance test, the  $\text{LiNi}_{0.5}\text{Co}_{0.2}\text{Mn}_{0.3}\text{O}_2$  (NCM523) commercial cathode material was opted due to the ester electrolyte we used with a wider voltage window. The NCM523 cathode electrode material was mixed with acetylene black and N-

methyl pyrrolidone (NMP) with a mass ratio of 8:1:1 and stirred overnight. Then, the slurry was evenly spread on the aluminum foil and dried in a 60  $^{\circ}\text{C}$  oven. After the overnight drying, the cathode composite was cut into a round disk for use. The CF and N-CF were predeposited with 5  $\text{mAh cm}^{-2}$  Li metal by electrochemical deposition as the negative electrode, and the NCM523 cathode material with an areal mass loading of 3.176  $\text{mg cm}^{-2}$  was used as the positive electrode. During the high loading of NCM523 cathode material preparation, the NCM523 cathode electrode material, acetylene black, and N-methyl pyrrolidone (NMP) were controlled with a mass ratio of 94:3:3. Then, the NCM523 cathode material with an areal mass loading of 16.254  $\text{mg cm}^{-2}$  (2.6  $\text{mAh cm}^{-2}$ ) was used as the positive electrode; the CF and N-CF were predeposited with 7.8  $\text{mAh cm}^{-2}$  Li metal, which indicated that the N/P ratio was controlled to be 3.

## RESULTS AND DISCUSSION

The cellulose fiber is an easily obtained experimental material and inherently possesses abundant pores and voids to adsorb particles to achieve the purpose of filtration, ensuring the penetration of an electrolyte and the rapid transport of  $\text{Li}^+$  ions. Furthermore, the voids can also relieve volume expansion of Li metal, thereby reducing the breakage of SEI. Combining the physical properties of CF and N-CF (Table S1), it can be calculated that when 3 and 5  $\text{mAh cm}^{-2}$  are deposited, the overall specific capacity of CF is decreased to 489 and 751  $\text{mAh g}^{-1}$  (the N-CF is decreased to 423 and 657  $\text{mAh g}^{-1}$ ), which can be seen in Table S2. As shown in Figure 1a, the cellulose fiber was immersed in the aqueous urea solution (nitrogen source) and annealed at a high temperature of 750  $^{\circ}\text{C}$  to obtain N-CF. After calcination treatment, the cellulose in the cellulose fiber is completely converted into 3D interconnected carbon fibers with high conductivity. Benefiting from the nitrogen doping effect, the N-CF exhibits better flexibility and mechanical strength than CF, which can maintain the structural integrity after cycling. To evaluate the morphology and structure of CF and N-CF, SEM images at different magnifications were collected, as shown in Figure 2.

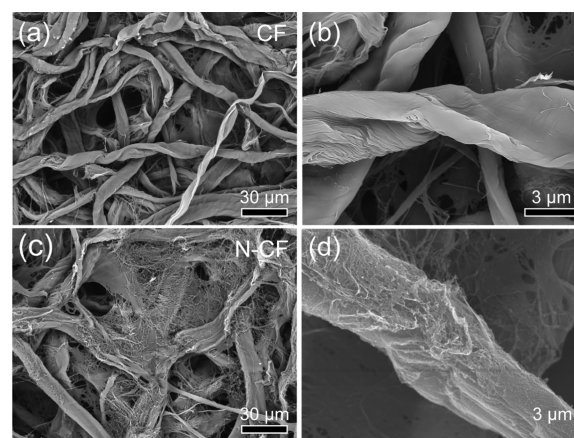


**Figure 2.** Different magnifications of SEM images of CF (a, b) and N-CF (c, d).

The diameter of carbon fibers approximately ranges from 5 to 10  $\mu\text{m}$ , as shown in Figure 2a,b. The cross-linked carbon wires constitute an excellent conductive network, which not only homogenize the electric field of the Li deposition process but also contribute to more uniform Li metal deposition.<sup>30</sup> After nitrogen doping, the 3D cross-linked structure of the CF has not been affected basically (Figure 2c,d), and a finer network

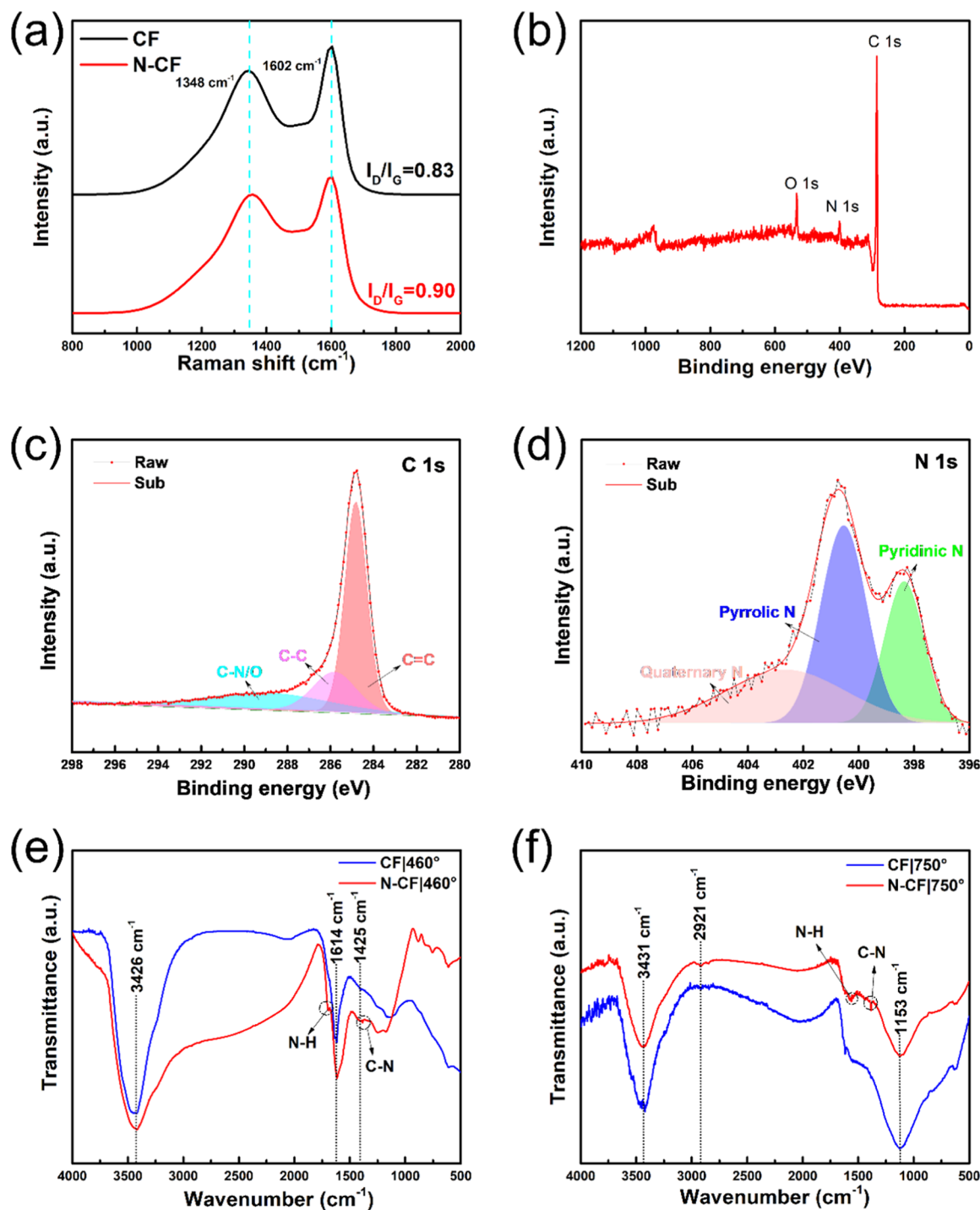


**Figure 3.** (a) Raman spectra of CF and N-CF. (b) The XPS spectra of the N-CF current collector. The (c) C 1s and (d) N 1s spectra of N-CF. The FTIR spectra of CF and N-CF calcined at the temperatures of (e) 460 °C and (f) 750 °C.

structure appears on the carbon wire surface, which does not appear in the CF without nitrogen doping. This indicates that nitrogen doping caused the fibrosis of the carbon wire surface. The fibrillation process improves the wettability of the electrolyte toward N-CF, which will be described in detail in the following discussion. In addition, the corresponding element distribution diagram shows that the nitrogen element was evenly distributed through the surface SEM images (Figure S1) and cross-section SEM images (Figure S2). The overall mass content of nitrogen was measured to be 6.09% using elemental analysis (Table S3). According to previous

literature reports, the nitrogen element can effectively induce the uniform deposition of Li metal.<sup>31</sup>

To obtain molecular structure information and different elements' valence states on the surface of the material, the Raman spectroscopy experiment and X-ray photoelectron spectroscopy were carried out, as shown in Figure 3. Raman spectroscopy can reveal the existence of heteroatom doping and characterize the graphitization degree of carbon materials.<sup>32</sup> In Figure 3a, both samples exhibit two distinct peaks at 1348 and 1602  $\text{cm}^{-1}$ , which correspond to the D and G bands in the carbon material, respectively. For the G band, it is

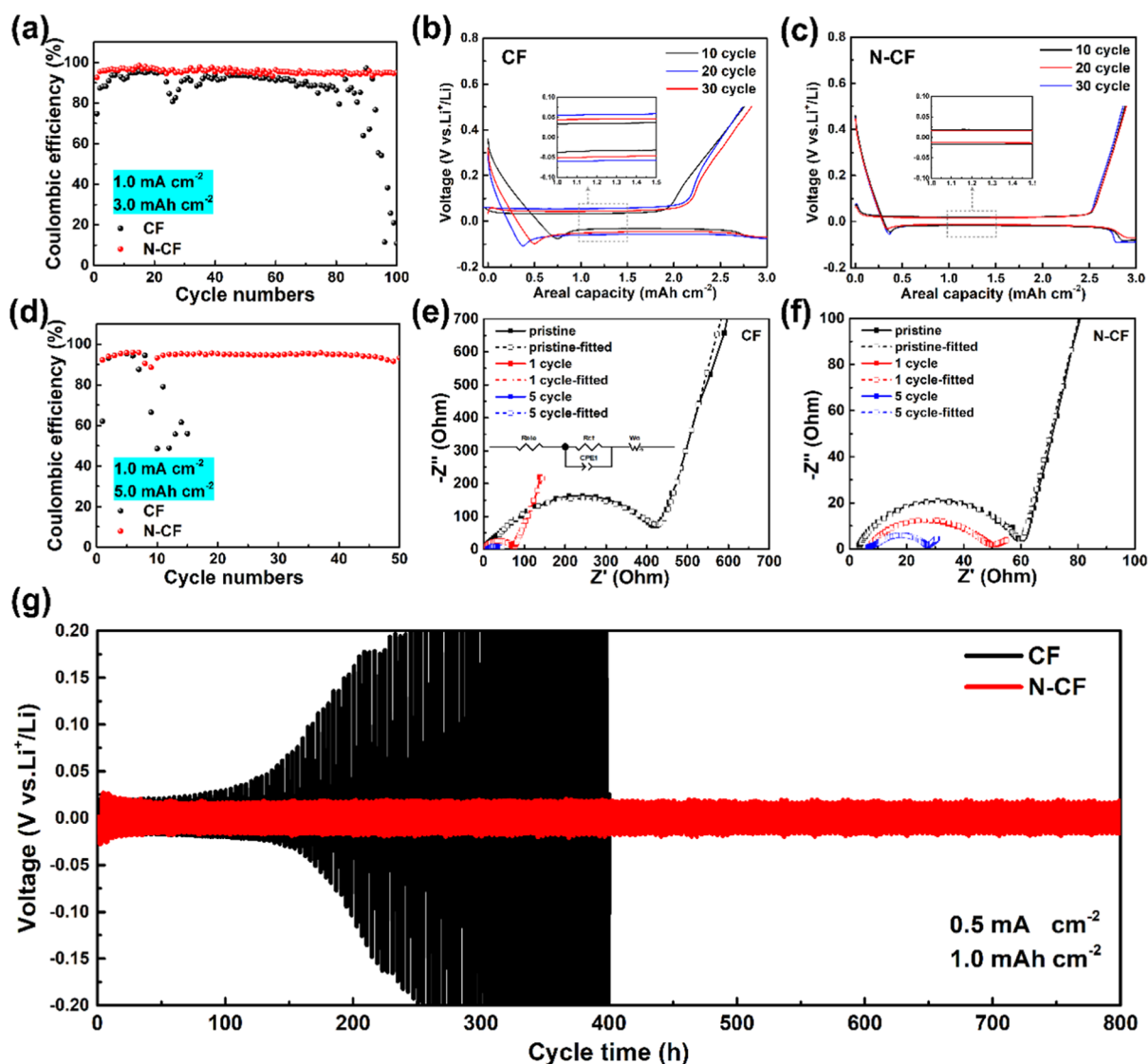


**Figure 4.** Half-cell cycling electrochemical performance with CF and N-CF. (a) The half-cell with the deposition capacity of  $3 \text{ mAh cm}^{-2}$ . The detailed voltage–capacity spectra of (b) CF and (c) N-CF at different cycles. (d) The half-cell with the deposition capacity of  $5 \text{ mAh cm}^{-2}$ . Comparison of EIS spectra with (e) CF and (f) N-CF after different cycles. (g) The symmetric cell cycling performance with the deposition capacity of  $1 \text{ mAh cm}^{-2}$  and deposition current of  $0.5 \text{ mA cm}^{-2}$ .

mainly attributed to the  $E_{2g}$  vibration mode of the  $sp^2$  bond in graphene carbon. For the D band, it mainly originates from the disorder caused by the  $sp^3$  defect site on the graphite plane. In this study, the D band can reflect the degree to which carbon atoms in the graphene layer are replaced by heteroatoms. Generally, the area ratio ( $I_D/I_G$ ) of the D band to the G band can be calculated for comparison. It can be clearly seen that the  $I_D/I_G$  ratio of the N-CF (0.90) is larger than that of the CF (0.83). It shows that the N-CF has a greater degree of defective atoms, indicating that the nitrogen atoms successfully replace part of the carbon atoms. In addition, the electronic conductivities of CF and N-CF were tested through a four-point probe power conductivity analyzer, and it was found that the conductivity of N-CF was  $2.32 \text{ S cm}^{-1}$ , about 6 times higher than that of CF ( $0.37 \text{ S cm}^{-1}$ ).<sup>33,34</sup> The N-CF current collector with higher electronic conductivity can strengthen the connection between the deposited Li metal and conductive matrix, thereby reducing the probability of dead Li generation.

The measurement results of XPS can show the chemical composition and valence state of the sample. It is obvious that

the peak corresponding to N 1s at  $400.8 \text{ eV}$  can be seen.<sup>35</sup> Moreover, the C 1s spectrum can be divided into three peaks located at  $284.8$ ,  $285.8$ , and  $288.2 \text{ eV}$ , corresponding to the  $\text{C}=\text{C}$ ,  $\text{C}-\text{C}$ , and  $\text{C}-\text{N/O}$  bond, respectively (Figure 3c). It is obvious that after adding urea, the N element successfully connects different polyacenes. In contrast, the N peak does not appear in the CF (Figure S3). Furthermore, the N 1s spectrum can be divided into three peaks fixed at  $398.4$ ,  $400.3$ , and  $402.1 \text{ eV}$ , corresponding to pyridinic nitrogen (pnN), pyrrolic nitrogen (prN), and quaternary N, respectively (Figure 3d). It has been proved in previous studies that pnN and prN possess higher binding energy with Li compared to carbon materials and copper substrates. It means that they can form stronger bonds with Li, and prN can absorb Lewis acidic Li ions in the electrolyte through acid–base interaction, thereby guiding the uniform deposition of metallic Li nuclei.<sup>36,37</sup>

To elucidate the role of urea in the cellulose carbonization process, the FTIR spectrum is shown in Figure 3e,f. According to previous reports, cellulose mainly undergoes dehydration and deoxygenation reactions below  $460 \text{ }^\circ\text{C}$ . Intramolecular

hydrogen bonds are broken and hydroxyl groups are dehydrated, resulting in various band structures such as benzene rings and aryl alkyl ethers. In the carbonization reaction, which is dominated by the deoxygenation reaction, the benzene ring structure undergoes a polyacene reaction to generate polyacene.<sup>38</sup> Therefore, the characteristic peaks of 1614 and 1425  $\text{cm}^{-1}$  appear in the infrared spectra at a calcination temperature of 460  $^{\circ}\text{C}$ , corresponding to the  $=\text{CH}$  in-plane deformation vibrations and  $\text{C}=\text{O}$  stretching vibrations in polyacene, respectively.<sup>39,40</sup> However, it does not appear in the FTIR spectrum at 750  $^{\circ}\text{C}$ , which shows that polyacene is an intermediate product in the calcination process. The peak displacements of 1653 and 1401  $\text{cm}^{-1}$  correspond to the  $\text{N}-\text{H}$  bending vibration and  $\text{C}-\text{N}$ , which corresponds to the bridging reaction of nitrogen between polyacenes, as mentioned in Figure 1b.<sup>41–44</sup> After the temperature increases to 750  $^{\circ}\text{C}$ , it is obvious that all of the original polyacene peaks disappear, and  $-\text{CO}$  stretching in a glucose pyran ring (1153  $\text{cm}^{-1}$ ),  $-\text{CH}$  stretching in  $\text{C}_6$ -methylene of a glucopyranose ring (2921  $\text{cm}^{-1}$ ), and  $-\text{OH}$  stretching in intramolecular hydrogen bonds (3431  $\text{cm}^{-1}$ ) can be seen.<sup>45,46</sup> However, after adding urea, the bridge reaction within the polyacene can be effectively carried out. The direct stable bridge between carbon and carbon is realized, thereby greatly improving the structural stability in the electrochemical process. Since the bridging reaction can connect linear organic molecules to form a network structure, the mechanical strength of the polymer can be greatly improved. In summary, the advantages of N-CF during Li metal deposition can be summarized as follows: (1) the highly conductive N-CF can homogenize the electric field around Li metal and reduce the local current density, which helps to reduce the polarization effect and delay the formation of Li dendrites; (2) the higher ratio of pnN and prN can contribute to the uniform deposition of Li metal and restrain the formation of Li dendrites, improving the cycle life of Li metal cells; and (3) the bridging reaction of nitrogen in the carbonization process of cellulose provides N-CF with excellent mechanical strength and flexibility, and guarantees cycle stability.

To investigate the cycling performance of CF and N-CF, the half-cell and symmetric cell test results are shown in Figure 4. Under the test conditions of 3 and 1  $\text{mA cm}^{-2}$ , the N-CF can maintain the high Coulombic efficiency (96%) and excellent cycling stability up to 100 cycles. In sharp contrast, the Coulombic efficiency of CF begins to decrease gradually after 23 cycles and exhibits a much lower value of only 80% at the 26th cycle (Figure 4a). The result reveals that although CF can reduce local current density while suppressing Li dendrites in early stage, the generated electrode/electrolyte interface is not stable, which may affect the long-term cycle stability. The capacity–voltage curve in the first five cycles shows that a certain amount of lithium is consumed during the activation process to form SEI (Figure S4). In the voltage–capacity curve, the voltage gap between the charging and discharging platforms can partly affect the stability and reversibility of the Li deposition interface. In Figure 4b, the CF initially exhibits an overpotential of 67 mV, which generally changes from 83 to 114 mV as the cycle deepens. The continuous change in the voltage gap also proves the instability of the electrode/electrolyte interface of CF. In contrast, the N-CF maintains a stable voltage gap of about 30 mV. This shows that the electrode/electrolyte interface and the structure of N-CF can maintain stability during the long cycle. During the half-cell

cycle test, the N-CF host initially inserted Li ions during the discharging process. When the voltage is reduced to below 0 V, the nucleation of Li metal starts to grow on N-CF. This phenomenon is common in carbon-based substrates because the intercalation potential of carbon is higher than the deposition voltage of Li metal.<sup>30,47,48</sup> As shown in Figure 4d, the CF fails after five cycles. In comparison, N-CF can maintain 95% of Coulombic efficiency during 50 cycles, showing that N-CF can still guarantee a stable long cycle with high Coulombic efficiency under high Li deposition capacity.

For the purpose of further exploring the interface difference of CF and N-CF during cycling, the EIS and corresponding fitting results are shown in Figure 4e,f. Before cycling, the CF sample exhibits much larger charge-transfer resistance (420  $\Omega$ ) compared to that of N-CF (60  $\Omega$ ), as shown in Figure S5. To explore this significant difference, the nitrogen adsorption–desorption isotherms of CF and N-CF were determined, as shown in Figure S6. The CF and N-CF current collectors exhibit specific surface areas of 631.50 and 595.87  $\text{m}^2 \text{g}^{-1}$ , which can take advantage of the 3D current collector. In addition, N-CF possesses a larger pore volume (0.0633  $\text{cm}^3 \text{g}^{-1}$ ) than that of CF (0.0445  $\text{cm}^3 \text{g}^{-1}$ ), which means that N-CF may retain more electrolyte. Investigated from the pore area distribution map, the number of N-CF in a mesoporous structure ( $>2 \text{ nm}$ ) is significantly more than CF. As the previous literature reported, mesopores are more conducive to the penetration of an electrolyte than micropores ( $<2 \text{ nm}$ ).<sup>49</sup> Therefore, the N-CF exhibits lower interface impedance without undergoing cycling. After going through one and five cycles, the interface impedance of the CF quickly decays to 74 and 42  $\Omega$ . The interface impedance of N-CF slowly decays to 50 and 30  $\Omega$ . Compared with the CF, N-CF can form a stable and low-impedance interface, which contributes to reducing the polarization and suppressing Li dendrites.

To further verify the superior electrochemical reversibility of N-CF, the CF and N-CF electrodes, which were predeposited with 5  $\text{mAh cm}^{-2}$  Li metal were assembled in symmetric cells. It can be seen from Figure 4g that the CF reaches 50 mV after 120 h and 200 mV after 240 h during the cycle. The rapid increase of the deposited overpotential indicates that the SEI generated on the CF is unstable and easily broken. The repeated crushing and generation of SEI easily results in the formation Li dendrites and accumulation of dead Li. Dead Li is bulky and electrochemically inert, thus causing a persistent increase in the polarization potential. On the contrary, the N-CF can maintain a very low polarization voltage (20 mV) and circulate steadily for 800 h, which demonstrated that N-CF can promote the formation of a more stable electrode/electrolyte interface because the pnN and prN in N-CF possess stronger binding energy with Li metal. From the enlarged voltage profiles of the symmetric Li metal cell at different cycling times, the stability of N-CF cycling performance can also be evaluated (Figure S7). Compared with CF, the N-CF can still have an intact structure after long cycling (Figure S8). The stable electrode/electrolyte interface can reduce the direct contact between the electrolyte and Li metal, thereby reducing the generation of dead Li. Overall, the N-CF can promote the formation of a more stable electrode/electrolyte interface while reducing the true current density of Li metal deposition. Therefore, it can effectively reduce the consumption of Li metal active materials and electrolytes while restraining the formation of Li dendrites, thus ameliorating the cycle life and Coulombic efficiency.

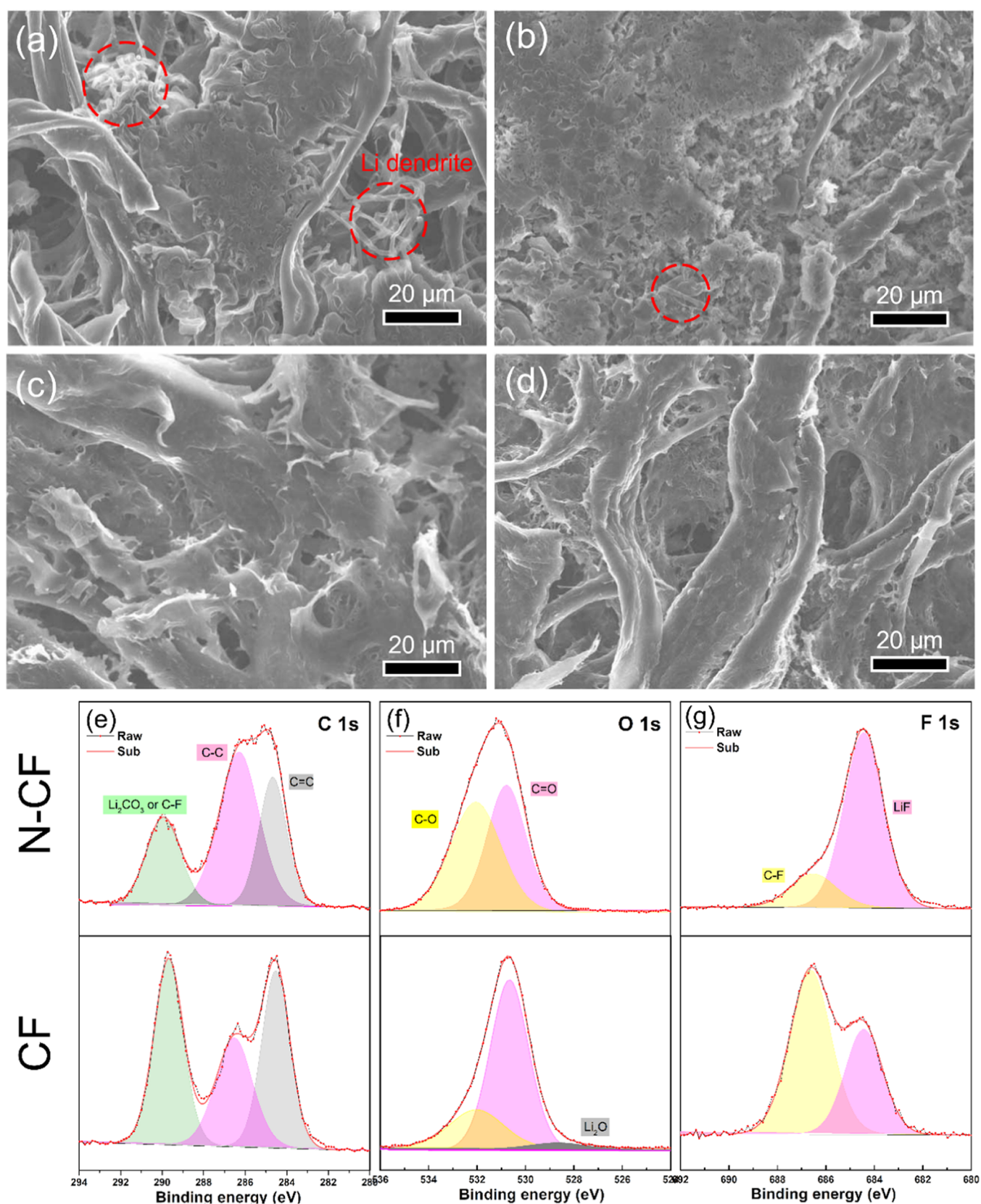


**Figure 5.** SEM images of the Li deposition morphology after different cycles. The SEM images of CF after (a) 1 cycle and (b) 10 cycles. The SEM images of N-CF after (c) 1 cycle and (d) 10 cycles. (e–g). The C 1s, O 1s, and F 1s spectra of the SEI position of CF and N-CF after 5 cycles.

To test the activity of N-CF on the Li metal deposition behavior, SEM was applied to characterize the Li deposition morphology of CF and N-CF after different cycles (Figure 5).

After undergoing only one cycle, the CF exhibits an uneven and broken morphology, which is also accompanied by the appearance of Li dendrites (Figure 5a). It indicated that the

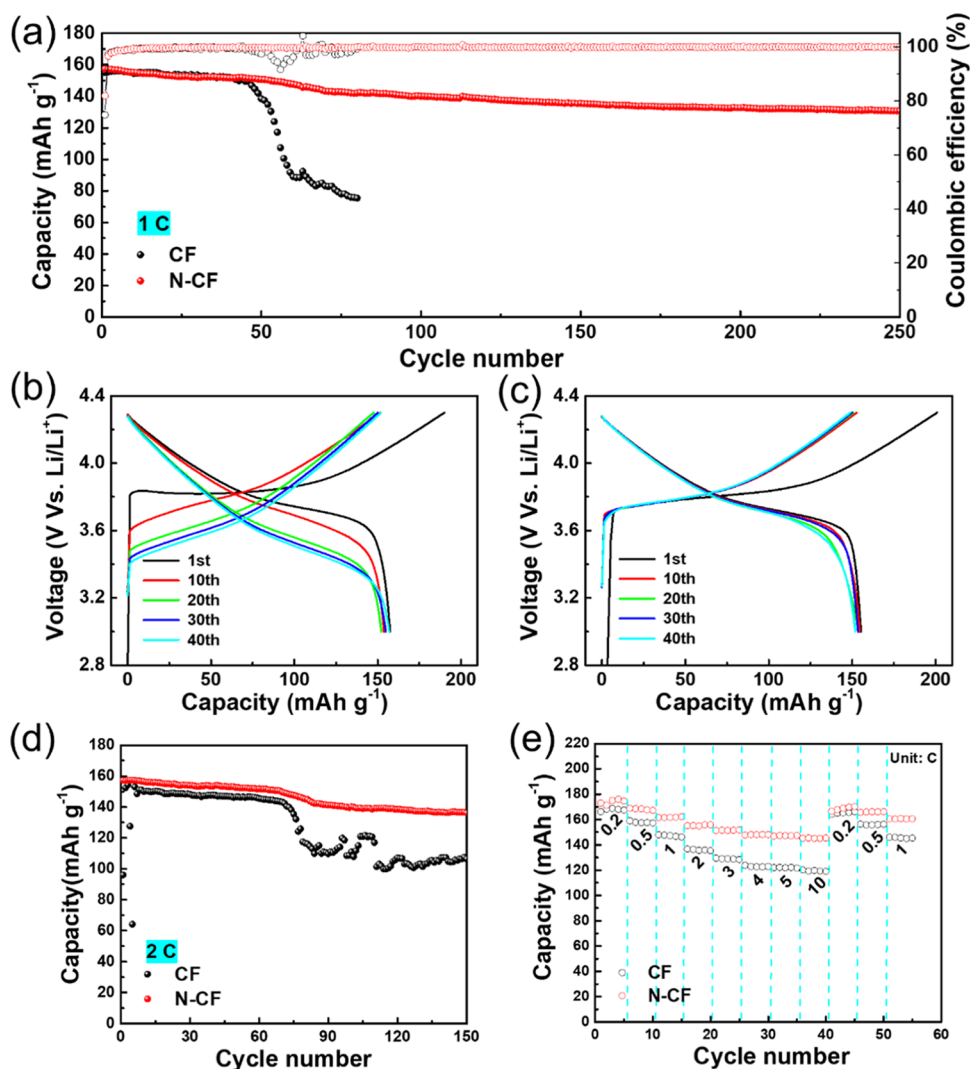


**Figure 6.** Electrochemical performance comparison with the NCM523 cathode material. (a) The long cycle performance with CF||Li and N-CF||Li electrodes at 1C. The voltage profiles of (b) CF||Li and (c) N-CF||Li electrodes at different cycles. (d) Cycling performance comparison at the charge–discharge rate of 2C. (e) The contrast in the electrochemical performance rate with CF||Li and N-CF||Li electrodes.

CF possesses low affinity with Li metal, and the electrode/electrolyte interface generated on the surface is very unstable. The layer of the interface was easily damaged by the volume expansion of Li metal, making Li ions preferentially deposited in these cracks, thus generating the Li dendrite morphology (Figure S9). In further magnified SEM images, when 10 mAh  $\text{cm}^{-2}$  Li metal is deposited (Figure S10), the trend of Li dendrites can be more clearly observed. By comparison, the N-CF current collector can induce Li metal deposition on the surface. As a result, it can ensure smooth deposition when depositing a larger amount of Li metal and alleviate the formation of Li dendrites. After 10 cycles, the CF shows a broken and loose Li deposition morphology (Figure 5b). The broken Li morphology is the dead Li formed after the Li dendrites break away from the Li metal matrix. The increase in dead Li not only increases the cell interfacial impedance but also generally aggravates the formation of Li dendrites. On the contrary, the N-CF can ensure Li metal deposition on its surface or in its voids, which can effectively relieve the volume expansion of Li metal (Figure 5c,d). The prN functional group in N-CF can induce uniform Li metal deposition, thereby reducing Li dendrites and promoting reduction of dead Li.

Above all, N-CF can induce uniform deposition of Li metal and relieve the volume expansion of Li metal so it can ensure the realization of a smooth Li deposition behavior.

To get deep insight into the electrode/electrolyte interface, the analysis of the SEI composition formed on CF and N-CF was carried out by XPS analysis. The fitted values of the C 1s spectrum can obviously be divided into three peaks corresponding to  $\text{Li}_2\text{CO}_3$  or C-F at 289.9 eV, C-C at 286.2 eV, and C=C at 284.8 eV, respectively (Figure 5e).<sup>50–53</sup> The N-CF with a larger proportion of oxygen-containing group peaks means that the surface SEI layer consisted of many components of  $\text{Li}_2\text{CO}_3$  and  $\text{ROCO}_2\text{Li}$ . Furthermore, the N-CF exhibits no obvious peak of  $\text{Li}_2\text{O}$  in the O 1s spectrum relative to the CF (Figure 5f). This shows that the SEI of N-CF can effectively block the contact between Li metal and the electrolyte, which is the main cause of  $\text{Li}_2\text{O}$  formation. In addition, the N-CF possesses a large proportion of LiF (684.4 eV) compared to the CF (Figure 5g).<sup>54</sup> In previous reports, it is confirmed that LiF is a very stable SEI component that is beneficial to relieve the formation of Li dendrites.<sup>55–57</sup> Consequently, the N-CF can promote formation of a stable SEI layer rich in LiF, helping to suppress Li dendrites. Due to

the stronger binding energy of pnN and prN with Li metal in N-CF, it can ensure the stability of SEI during prolonged cycling. Moreover, the prN can effectively guide the uniform Li deposition, and even the Li metal surface further promotes a stable electrode/electrolyte interface. Therefore, excellent cycle stability of Li metal cells can be achieved.

To verify the superiority of the N-CF in real Li-metal-based cell, the full cell was assembled and tested at different current densities (Figure 6). Due to the ester, the electrolyte can withstand higher working voltage compared with the traditional ether electrolyte, which possesses higher affinity for Li metal. Therefore, the NCM523 material that can withstand higher voltages was selected as the cathode material. According to Figure 6a, under the condition that the current density is  $0.508 \text{ mA cm}^{-2}$  (1C), the CF||Li electrode initially exhibits a specific capacity of  $155.2 \text{ mAh g}^{-1}$ . However, the Li metal on the anode side is consumed and cannot provide sufficient Li after 50 cycles. The capacity began to decay rapidly. As a comparison, N-CF||Li initially exhibited a specific capacity of  $157.3 \text{ mAh g}^{-1}$ , which was able to maintain 83.1% ( $130.7 \text{ mAh g}^{-1}$ ) after 250 cycles and maintained high stable Coulombic efficiency of 99.9%. This shows that N-CF can effectively reduce the Li metal loss in the case of a limited amount of the Li metal, thereby improving the cycling life of the full cell. During the full-cell test, the initial Coulombic efficiencies of CF and N-CF are 80.9 and 81.9%, respectively (Figure S11). Therefore, due to the larger initial polarization of the CF full cell, resulting in a higher charging voltage, the electrode/electrolyte interface gradually stabilized after a series of cycles, so this phenomenon disappeared. During the charge–discharge curve, the voltage drop when it reaches half of the discharge capacity can be used to reflect the polarization during the full-cell charge/discharge process.<sup>58–60</sup> It can be easily seen that the CF||Li electrode cannot maintain the typical curve of the NCM523 cathode electrode material during the long cycle. With the cycle deepening, the detrimental voltage drop gradually increases due to the increased polarization and material structural degradation. The N-CF||Li electrode delivers an inappreciable voltage drop while maintaining very high capacity retention (Table S4). This indicates that the N-CF can construct a stable electrode/electrolyte interface and keep the structural stability, reducing the dead Li and reducing the overall polarization of the cell. When further testing the electrochemical performance at 2 C, the N-CF||Li electrode still exhibited very high charge–discharge reversible efficiency and exhibited a high capacity retention rate of 86.6% after 150 cycles. Unfortunately, the CF||Li failed after 70 cycles. More importantly, N-CF||Li shows the overwhelming advantage in the rate test. It is worth mentioning that N-CF exhibits capacity of 146.2 and 144.3  $\text{mAh g}^{-1}$  at 5C and 10C, respectively. On the other hand, CF only releases specific capacities of 122.3 and 119.0  $\text{mAh g}^{-1}$ . To verify the advantages of the N-CF host in cell practicality, the full-cell test was conducted under higher loading conditions. The cathode electrode uses an areal capacity of  $2.6 \text{ mAh cm}^{-2}$  ( $16.254 \text{ mg cm}^{-2}$ ), and the anode electrode is predeposited with  $7.8 \text{ mAh cm}^{-2}$ . The capacity ratio of the positive electrode to the negative electrode is strictly controlled to be 3, and the rate density is designed to be  $2.6 \text{ mA cm}^{-2}$  (1.0C). Larger current density places higher requirements on the ion transport capacity of the electrode/electrolyte interface. As shown in Figure S12, the capacity with the N-CF host does not change much after 20 cycles, while the capacity retention

with the CF host decays to 80%. It confirms that the N-CF can promote a stable and conducive Li-ion transmission electrode/electrolyte interface so it can have good performance in the rate test. All in all, the N-CF can contribute to constructing a stable and favorable electrode/electrolyte interface and the structural stability enabled by the bridge reaction of nitrogen. As a result, the high capacity retention rate under the long cycle can be realized, especially at a high-rate electrochemical test.

## CONCLUSIONS

In this work, the N-CF with a multidimensional network structure was successfully synthesized through a simple calcination reaction as a Li metal current collector. The characterization results show that the nitrogen element is evenly distributed in the conductive network of the CF, and the nitrogen doping achieves the fibrosis of the carbon wire surface. As a result, the N-CF possesses a richer mesoporous structure, which is conducive to the penetration of an electrolyte. The results of the Li deposition morphology show that N-CF can reduce the generation of Li dendrites and dead Li. When applied to full-cell testing, the N-CF||Li electrode can maintain a capacity of up to 83.1% and Coulombic efficiency of 99.9% after 250 cycles, while the CF||Li electrode failed after 50 cycles. Moreover, N-CF||Li exhibits outstanding superiority in high-rate cycling tests. All of these improvements can attribute to the N-CF's ability to promote the establishment of a stable conducive Li-ion transmission electrode/electrolyte interface and the structural stability provided by the bridge reaction of nitrogen between polyacenes. The N-CF not only reduces the local Li deposition current density to suppress the formation of Li dendrites but also reduces the generation of dead Li and overall polarization by establishing a stable electrode/electrolyte interface. Therefore, the N-CF enables the long-time cycling and high stripping/dropping efficiency to be achieved simultaneously. Our work provides a method for the research direction of combining multiple current collectors and constructing a stable electrode/electrolyte interface.

## ASSOCIATED CONTENT

### Supporting Information

The Supporting Information is available free of charge at <https://pubs.acs.org/doi/10.1021/acssuschemeng.0c08572>.

Element mapping (Figure S1); the cross-sectional SEM image (Figure S2); XPS spectra (Figure S3); detailed voltage–capacity spectra (Figure S4); enlarged EIS spectra (Figure S5); nitrogen adsorption–desorption isotherms (Figure S6); enlarged voltage profiles of the symmetric Li metal cell (Figure S7); image comparison (Figure S8); the detailed SEM images of Li deposition morphology with the CF current collector after (a) 1 cycle and (b) 10 cycles (Figure S9); different magnification SEM figures of Li metal morphologies with CF (a–c) and N-CF (d–f) current collectors when deposited with  $10 \text{ mAh cm}^{-2}$  Li metal (Figure S10); the enlarged voltage profile of CF and N-CF electrodes at the first cycle (Figure S11); the tests of Li||NCM523 full cells at 1.0C with capacity ratios of anode/cathode of 3 (NCM loading of  $16.254 \text{ mg cm}^{-2}$ ) (Figure S12); the physical properties of CF and N-CF current collectors (Table S1); the specific capacity of the composite anode

with CF (Table S2); mass content of different element in N-CF (Table S3); and voltage delay (Table S4) (PDF)

## AUTHOR INFORMATION

### Corresponding Authors

**Yang Yang** – School of Chemical Engineering and Light Industry, Guangdong University of Technology, Guangzhou 510006, China; Email: yangyang@gdut.edu.cn

**Jinbao Zhao** – State Key Lab of Physical Chemistry of Solid Surfaces, Collaborative Innovation Centre of Chemistry for Energy Materials, State-Province Joint Engineering Laboratory of Power Source Technology for New Energy Vehicle, Engineering Research Center of Electrochemical Technology, Ministry of Education, College of Chemistry and Chemical Engineering, Xiamen University, Xiamen 361005, China; [orcid.org/0000-0002-2753-7508](https://orcid.org/0000-0002-2753-7508); Email: jbzhaoy@xmu.edu.cn

### Authors

**Zhipeng Wen** – State Key Lab of Physical Chemistry of Solid Surfaces, Collaborative Innovation Centre of Chemistry for Energy Materials, State-Province Joint Engineering Laboratory of Power Source Technology for New Energy Vehicle, Engineering Research Center of Electrochemical Technology, Ministry of Education, College of Chemistry and Chemical Engineering, Xiamen University, Xiamen 361005, China

**Huiyang Li** – State Key Lab of Physical Chemistry of Solid Surfaces, Collaborative Innovation Centre of Chemistry for Energy Materials, State-Province Joint Engineering Laboratory of Power Source Technology for New Energy Vehicle, Engineering Research Center of Electrochemical Technology, Ministry of Education, College of Chemistry and Chemical Engineering, Xiamen University, Xiamen 361005, China

**Jiaxiang Liu** – College of Energy & School of Energy Research, Xiamen University, Xiamen 361102, Fujian, China

Complete contact information is available at:  
<https://pubs.acs.org/10.1021/acssuschemeng.0c08572>

### Notes

The authors declare no competing financial interest.

## ACKNOWLEDGMENTS

This work was supported by the National Natural Science Foundation of China (No. 21875195) and the Fundamental Research Funds for the Central Universities (No. 20720190040).

## REFERENCES

- (1) Tarascon, J. M.; Armand, M. Issues and challenges facing rechargeable lithium batteries. *Nature* **2001**, *414*, 359–367.
- (2) Dunn, B.; Kamath, H.; Tarascon, J. M. Electrical energy storage for the grid: a battery of choices. *Science* **2011**, *334*, 928–935.
- (3) Yang, Y.; Zhu, H.; Xiao, J.; Geng, H.; Zhang, Y.; Zhao, J.; Li, G.; Wang, X. L.; Li, C. C.; Liu, Q. Achieving Ultrahigh-Rate and High-Safety Li(+) Storage Based on Interconnected Tunnel Structure in Micro-Size Niobium Tungsten Oxides. *Adv. Mater.* **2020**, *32*, No. 1905295.
- (4) Xu, J.-J.; Liu, Q. C.; Yu, Y.; Wang, J.; Yan, J. M.; Zhang, X. B. In Situ Construction of Stable Tissue-Directed/Reinforced Bifunctional

Separator/Protection Film on Lithium Anode for Lithium-Oxygen Batteries. *Adv. Mater.* **2017**, *29*, No. 1606552.

- (5) Wang, J.; Yin, Y. B.; Liu, T.; Yang, X. Y.; Chang, Z. W.; Zhang, X. B. Hybrid electrolyte with robust garnet-ceramic electrolyte for lithium anode protection in lithium-oxygen batteries. *Nano Res.* **2018**, *11*, 3434–3441.

- (6) Ma, J.-L.; Meng, F. L.; Yu, Y.; Liu, D. P.; Yan, J. M.; Zhang, Y.; Zhang, X. B.; Jiang, Q. Prevention of dendrite growth and volume expansion to give high-performance aprotic bimetallic Li-Na alloy-O<sub>2</sub> batteries. *Nat. Chem.* **2019**, *11*, 64–70.

- (7) Ji, X.; Nazar, L. F. Advances in Li–S batteries. *J. Mater. Chem.* **2010**, *20*, 9821–9826.

- (8) Chen, Y.; Luo, Y.; Zhang, H. Z.; Qu, C.; Zhang, H. M.; Li, X. F. The Challenge of Lithium Metal Anodes for Practical Applications. *Small Methods* **2019**, *3*, No. 1800551.

- (9) Tikekar, M. D.; Choudhury, S.; Tu, Z. Y.; Archer, L. A. Design principles for electrolytes and interfaces for stable lithium-metal batteries. *Nat. Energy* **2016**, *1*, 1–7.

- (10) Liu, H.; Cheng, X.-B.; Jin, Z.; Zhang, R.; Wang, G.; Chen, L.-Q.; Liu, Q.-B.; Huang, J.-Q.; Zhang, Q. Recent advances in understanding dendrite growth on alkali metal anodes. *EnergyChem* **2019**, *1*, No. 100003.

- (11) Fang, C.; Li, J.; Zhang, M.; Zhang, Y.; Yang, F.; Lee, J. Z.; Lee, M. H.; Alvarado, J.; Schroeder, M. A.; Yang, Y.; Lu, B.; Williams, N.; Ceja, M.; Yang, L.; Cai, M.; Gu, J.; Xu, K.; Wang, X.; Meng, Y. S. Quantifying inactive lithium in lithium metal batteries. *Nature* **2019**, *572*, 511–515.

- (12) Ding, F.; Xu, W.; Graff, G. L.; Zhang, J.; Sushko, M. L.; Chen, X.; Shao, Y.; Engelhard, M. H.; Nie, Z.; Xiao, J.; Liu, X.; Sushko, P. V.; Liu, J.; Zhang, J. G. Dendrite-free lithium deposition via self-healing electrostatic shield mechanism. *J. Am. Chem. Soc.* **2013**, *135*, 4450–4456.

- (13) Li, W.; Yao, H.; Yan, K.; Zheng, G.; Liang, Z.; Chiang, Y. M.; Cui, Y. The synergetic effect of lithium polysulfide and lithium nitrate to prevent lithium dendrite growth. *Nat. Commun.* **2015**, *6*, No. 7436.

- (14) Yang, Y.; Xiong, J.; Lai, S.; Zhou, R.; Zhao, M.; Geng, H.; Zhang, Y.; Fang, Y.; Li, C.; Zhao, J. Vinyl Ethylene Carbonate as an Effective SEI-Forming Additive in Carbonate-Based Electrolyte for Lithium-Metal Anodes. *ACS Appl. Mater. Interfaces* **2019**, *11*, 6118–6125.

- (15) Chen, K.; Pathak, R.; Gurung, A.; Adhamash, E. A.; Bahrami, B.; He, Q. Q.; Qiao, H.; Smirnova, A. L.; Wu, J. J.; Qiao, Q. Q.; Zhou, Y. Flower-shaped lithium nitride as a protective layer via facile plasma activation for stable lithium metal anodes. *Energy Storage Mater.* **2019**, *18*, 389–396.

- (16) Lin, Y.; Wen, Z.; Liu, J.; Wu, D.; Zhang, P.; Zhao, J. Constructing a uniform lithium iodide layer for stabilizing lithium metal anode. *J. Energy Chem.* **2021**, *55*, 129–135.

- (17) Lang, J.; Long, Y.; Qu, J.; Luo, X.; Wei, H.; Huang, K.; Zhang, H.; Qi, L.; Zhang, Q.; Li, Z.; Wu, H. One-pot solution coating of high quality LiF layer to stabilize Li metal anode. *Energy Storage Mater.* **2019**, *16*, 85–90.

- (18) Gu, Y.; Wang, W. W.; Li, Y. J.; Wu, Q. H.; Tang, S.; Yan, J. W.; Zheng, M. S.; Wu, D. Y.; Fan, C. H.; Hu, W. Q.; Chen, Z. B.; Fang, Y.; Zhang, Q. H.; Dong, Q. F.; Mao, B. W. Designable ultra-smooth ultrathin solid-electrolyte interphases of three alkali metal anodes. *Nat. Commun.* **2018**, *9*, No. 1339.

- (19) Gu, Y.; Xu, H. Y.; Zhang, X. G.; Wang, W. W.; He, J. W.; Tang, S.; Yan, J. W.; Wu, D. Y.; Zheng, M. S.; Dong, Q. F.; Mao, B. W. Lithiophilic Faceted Cu(100) Surfaces: High Utilization of Host Surface and Cavities for Lithium Metal Anodes. *Angew. Chem., Int. Ed.* **2019**, *58*, 3092–3096.

- (20) Yang, Y.; Xiong, J.; Zeng, J.; Huang, J.; Zhao, J. VGCF 3D conducting host coating on glass fiber filters for lithium metal anodes. *Chem. Commun.* **2018**, *54*, 1178–1181.

- (21) Wen, Z.; Peng, Y. Y.; Cong, J. L.; Hua, H. M.; Lin, Y. X.; Xiong, J.; Zeng, J.; Zhao, J. B. A stable artificial protective layer for high capacity dendrite-free lithium metal anode. *Nano Res.* **2019**, *12*, 2535–2542.

- (22) Shi, Y.; Wang, Z. B.; Gao, H.; Niu, J. Z.; Ma, W. S.; Qin, J. Y.; Peng, Z. Q.; Zhang, Z. H. A self-supported, three-dimensional porous copper film as a current collector for advanced lithium metal batteries. *J. Mater. Chem. A* **2019**, *7*, 1092–1098.
- (23) Liu, Y.; Qin, X.; Liu, F.; Huang, B.; Zhang, S.; Kang, F.; Li, B. Basal Nanosuit of Graphite for High-Energy Hybrid Li Batteries. *ACS Nano* **2020**, *14*, 1837–1845.
- (24) Liu, Y.; Yin, X.; Shen, X.; Zou, P.; Qin, X.; Yang, C.; Zhang, Q.; Kang, F.; Chen, G.; Li, B. Horizontal Stress Release for Protuberance-Free Li Metal Anode. *Adv. Funct. Mater.* **2020**, *30*, No. 2002522.
- (25) Liu, Y.; Qin, X. Y.; Zhang, S. Q.; Huang, Y. L.; Kang, F. Y.; Chen, G. H.; Li, B. H. Oxygen and nitrogen co-doped porous carbon granules enabling dendrite-free lithium metal anode. *Energy Storage Mater.* **2019**, *18*, 320–327.
- (26) Liu, Y.; Qin, X. Y.; Zhang, S. Q.; Zhang, L. H.; Kang, F. Y.; Chen, G. H.; Duan, X. F.; Li, B. H. A scalable slurry process to fabricate a 3D lithiophilic and conductive framework for a high performance lithium metal anode. *J. Mater. Chem. A* **2019**, *7*, 13225–13233.
- (27) Shi, P.; Li, T.; Zhang, R.; Shen, X.; Cheng, X. B.; Xu, R.; Huang, J. Q.; Chen, X. R.; Liu, H.; Zhang, Q. Lithiophilic LiC<sub>6</sub> Layers on Carbon Hosts Enabling Stable Li Metal Anode in Working Batteries. *Adv. Mater.* **2019**, *31*, No. 1807131.
- (28) Shen, X.; Cheng, X.; Shi, P.; Huang, J.; Zhang, X.; Yan, C.; Li, T.; Zhang, Q. Lithium–matrix composite anode protected by a solid electrolyte layer for stable lithium metal batteries. *J. Energy Chem.* **2019**, *37*, 29–34.
- (29) Yan, C.; Yuan, H.; Park, H. S.; Huang, J. Q. Perspective on the critical role of interface for advanced batteries. *J. Energy Chem.* **2020**, *47*, 217–220.
- (30) Zuo, T.-T.; Wu, X. W.; Yang, C. P.; Yin, Y. X.; Ye, H.; Li, N. W.; Guo, Y. G. Graphitized Carbon Fibers as Multifunctional 3D Current Collectors for High Areal Capacity Li Anodes. *Adv. Mater.* **2017**, *29*, No. 1700389.
- (31) Kim, M. S.; Ryu, J.-H.; Deepika; Lim, Y. R.; Nah, I. W.; Lee, K.-R.; Archer, L. A.; Il Cho, W. Langmuir–Blodgett artificial solid-electrolyte interphases for practical lithium metal batteries. *Nat. Energy* **2018**, *3*, 889–898.
- (32) Wang, B.; Ji, L. L.; Yu, Y. L.; Wang, N. X.; Wang, J.; Zhao, J. B. A simple and universal method for preparing N, S co-doped biomass derived carbon with superior performance in supercapacitors. *Electrochim. Acta* **2019**, *309*, 34–43.
- (33) Luo, Z.; Lim, S. H.; Tian, Z. Q.; Shang, J. Z.; Lai, L. F.; MacDonald, B.; Fu, C.; Shen, Z. X.; Yu, T.; Lin, J. Y. Pyridinic N doped graphene: synthesis, electronic structure, and electrocatalytic property. *J. Mater. Chem.* **2011**, *21*, 8038–8044.
- (34) Li, S.-M.; Yang, S. Y.; Wang, Y. S.; Tsai, H. P.; Tien, H. W.; Hsiao, S. T.; Liao, W. H.; Chang, C. L.; Ma, C. C. M.; Hu, C. C. N-doped structures and surface functional groups of reduced graphene oxide and their effect on the electrochemical performance of supercapacitor with organic electrolyte. *J. Power Sources* **2015**, *278*, 218–229.
- (35) Xie, Y.; Fang, L.; Cheng, H. W.; Hu, C. J.; Zhao, H. B.; Xu, J. Q.; Fang, J. H.; Lu, X. G.; Zhang, J. J. Biological cell derived N-doped hollow porous carbon microspheres for lithium–sulfur batteries. *J. Mater. Chem. A* **2016**, *4*, 15612–15620.
- (36) Zhang, R.; Chen, X. R.; Chen, X.; Cheng, X. B.; Zhang, X. Q.; Yan, C.; Zhang, Q. Lithiophilic Sites in Doped Graphene Guide Uniform Lithium Nucleation for Dendrite-Free Lithium Metal Anodes. *Angew. Chem., Int. Ed.* **2017**, *56*, 7764–7768.
- (37) Chen, X.; Chen, X. R.; Hou, T. Z.; Li, B. Q.; Cheng, X. B.; Zhang, R.; Zhang, Q. Lithiophilicity chemistry of heteroatom-doped carbon to guide uniform lithium nucleation in lithium metal anodes. *Sci. Adv.* **2019**, *5*, No. eaau7728.
- (38) Shafizadeh, F.; Sekiguchi, Y. Development of aromaticity in cellulosic chars. *Carbon* **1983**, *21*, 511–516.
- (39) Marchessault, R. H.; Liang, C. Y. Infrared spectra of crystalline polysaccharides (III): Mercerized cellulose. *J. Polym. Sci. A* **1960**, *43*, 71–84.
- (40) Popescu, C. M.; Popescu, M. C.; Vasile, C. Structural analysis of photodegraded lime wood by means of FT-IR and 2D IR correlation spectroscopy. *Int. J. Biol. Macromol.* **2011**, *48*, 667–675.
- (41) Zheng, M.; Liu, Y. L.; Xiao, Y.; Zhu, Y.; Guan, Q.; Yuan, D. S.; Zhang, J. X. An Easy Catalyst-Free Hydrothermal Method to Prepare Monodisperse Carbon Microspheres on a Large Scale. *J. Phys. Chem. C* **2009**, *113*, 8455–8459.
- (42) Xie, H.-M.; Wang, R. S.; Ying, J. R.; Zhang, L. Y.; Jalbout, A. F.; Yu, H. Y.; Yang, G. L.; Pan, X. M.; Su, Z. M. Optimized LiFePO<sub>4</sub>–Polyacene Cathode Material for Lithium-Ion Batteries. *Adv. Mater.* **2006**, *18*, 2609–2613.
- (43) Chen, Z.; Xu, M.; Zhu, H. L.; Xie, T.; Wang, W. H.; Zhao, Q. F. Enhanced electrochemical performance of polyacene coated LiMn<sub>2</sub>O<sub>3</sub>.95F<sub>0.05</sub> for lithium ion batteries. *Appl. Surf. Sci.* **2013**, *286*, 177–183.
- (44) Chen, Z.; Du, B. L.; Xu, M.; Zhu, H. L.; Li, L. J.; Wang, W. H. Polyacene coated carbon/LiFePO<sub>4</sub> cathode for Li ion batteries: Understanding the stabilized double coating structure and enhanced lithium ion diffusion kinetics. *Electrochim. Acta* **2013**, *109*, 262–268.
- (45) Gardner, K. H.; Blackwell, J. The Structure of Native Cellulose. *Biopolymers* **1974**, *13*, 1975–2001.
- (46) Kang, C. Y.; Marchessault, R. H. Infrared spectra of crystalline polysaccharides (II): Native celluloses in the region from 640 to 1700 cm<sup>-1</sup>. *J. Polym. Sci. A* **1959**, *39*, 269–278.
- (47) Yang, Y.; Zhao, M.; Geng, H.; Zhang, Y.; Fang, Y.; Li, C.; Zhao, J. Three-Dimensional Graphene/Ag Aerogel for Durable and Stable Li Metal Anodes in Carbonate-Based Electrolytes. *Chem. - Eur. J.* **2019**, *25*, 5036–5042.
- (48) Kang, H.-K.; Woo, S. G.; Kim, J. H.; Lee, S. R.; Lee, D. G.; Yu, J. S. Three-dimensional monolithic corrugated graphene/Ni foam for highly stable and efficient Li metal electrode. *J. Power Sources* **2019**, *413*, 467–475.
- (49) Ji, L.; Wang, B.; Yu, Y. L.; Wang, N. X.; Zhao, J. B. N, S co-doped biomass derived carbon with sheet-like microstructures for supercapacitors. *Electrochim. Acta* **2020**, *331*, No. 135348.
- (50) Yang, Y.; Xiao, J.; Liu, C.; Chen, D.; Geng, H.; Zhang, Y.; Zhao, J.; Li, C. C.; He, W. Uniform Li Plating/Stripping within Ni Macropore Arrays Enabled by Regulated Electric Field Distribution for Ultra-Stable Li-Metal Anodes. *iScience* **2020**, *23*, No. 101089.
- (51) Zhang, G.; Lin, K.; Qin, X.; Zhang, L.; Li, T.; Lv, F.; Xia, Y.; Han, W.; Kang, F.; Li, B. Electrospayed Robust Graphene Layer Constructing Ultrastable Electrode Interface for High-Voltage Lithium-Ion Batteries. *ACS Appl. Mater. Interfaces* **2020**, *12*, 37034–37046.
- (52) Li, Z.; Lv, W.; Zhang, C.; Li, B.; Kang, F.; Yang, Q.-H. A sheet-like porous carbon for high-rate supercapacitors produced by the carbonization of an eggplant. *Carbon* **2015**, *92*, 11–14.
- (53) Wang, Q.; Yao, Z.; Zhao, C.; Verhallen, T.; Tabor, D. P.; Liu, M.; Ooms, F.; Kang, F.; Aspuru-Guzik, A.; Hu, Y. S.; Wagemaker, M.; Li, B. Interface chemistry of an amide electrolyte for highly reversible lithium metal batteries. *Nat. Commun.* **2020**, *11*, No. 4188.
- (54) Zhang, X.-Q.; Cheng, X. B.; Chen, X.; Yan, C.; Zhang, Q. Fluoroethylene Carbonate Additives to Render Uniform Li Deposits in Lithium Metal Batteries. *Adv. Funct. Mater.* **2017**, *27*, No. 1605989.
- (55) Li, T.; Zhang, X. Q.; Shi, P.; Zhang, Q. Fluorinated Solid-Electrolyte Interphase in High-Voltage Lithium Metal Batteries. *Joule* **2019**, *3*, 2647–2661.
- (56) Markevich, E.; Salitra, G.; Aurbach, D. Fluoroethylene Carbonate as an Important Component for the Formation of an Effective Solid Electrolyte Interphase on Anodes and Cathodes for Advanced Li-Ion Batteries. *ACS Energy Lett.* **2017**, *2*, 1337–1345.
- (57) Pathak, R.; Chen, K.; Gurung, A.; Reza, K. M.; Bahrami, B.; Pokharel, J.; Baniya, A.; He, W.; Wu, F.; Zhou, Y.; Xu, K.; Qiao, Q. Q. Fluorinated hybrid solid-electrolyte-interphase for dendrite-free lithium deposition. *Nat. Commun.* **2020**, *11*, No. 93.
- (58) Zou, L.; Liu, Z. Y.; Zhao, W. G.; Jia, H. P.; Zheng, J. M.; Yang, Y.; Wang, G. F.; Zhang, J. G.; Wang, C. M. Solid–Liquid Interfacial Reaction Triggered Propagation of Phase Transition from Surface into

Bulk Lattice of Ni-Rich Layered Cathode. *Chem. Mater.* **2018**, *30*, 7016–7026.

(59) Zhao, W.; Zou, L.; Zheng, J.; Jia, H.; Song, J.; Engelhard, M. H.; Wang, C.; Xu, W.; Yang, Y.; Zhang, J. G. Simultaneous Stabilization of LiNi<sub>0.76</sub> Mn<sub>0.14</sub> Co<sub>0.10</sub> O<sub>2</sub> Cathode and Lithium Metal Anode by Lithium Bis(oxalato)borate as Additive. *ChemSusChem* **2018**, *11*, 2211–2220.

(60) Fan, X.; Hu, G. R.; Zhang, B.; Ou, X.; Zhang, J. F.; Zhao, W. G.; Jia, H. P.; Zou, L. F.; Li, P.; Yang, Y. Crack-free single-crystalline Ni-rich layered NCM cathode enable superior cycling performance of lithium-ion batteries. *Nano Energy* **2020**, *70*, No. 104450.